Computational Mechanics
https://doi.org/10.1007/s00466-024-02488-y

ORIGINAL PAPER

# Digital twin of surface acoustic wave transceivers for a computational design of an optimal wave guiding layer thickness

**Ufuk Tan Baler**[1] · **Ali Fethi Okyar**[1] · **Bilen Emek Abali**[2]

Received: 3 December 2023 / Accepted: 15 April 2024


**Abstract**
Detection of biomarkers is exploited in lab-on-a-chip devices by means of Love type Surface Acoustic Waves (SAW). Finger type arrangement of electrodes, used for InterDigital-Transducers (IDT), perform well to create and detect SAW by using electro-mechanical coupling. Efficiency of such a transceiver depends on design parameters such as chosen material orientation, thickness, placement of electrodes. An optimized design reduces production costs, hence, we need a digital twin of the device with multiphysics simulations that compute deformation and electric field. In this study, we develop a framework with the open-source package called FEniCS for modal and transient analyses of IDTs by using the Finite Element Method (FEM). Specifically, we discuss all possible sensor design parameters and propose a computational design guideline that determines the "best" thickness parameter by maximizing mass sensitivity, thus, efficiency for a Love surface acoustic wave sensor.

**Keywords** Lab-on-a-chip · Love-wave · Optimization · Mass-sensitivity · FEM · IDT

## 1 Introduction

Among Surface Acoustic Waves (SAW), Love wave is a subset of horizontally polarized shear waves that is utilized widely for detecting biomarkers in microfluidics [1–3]. Owing to the wave confinement via the so-called guiding layer on a substrate, such devices that utilize Love waves have better performance as depicted in Fig. 1. Provided by the right combination of a substrate with a relatively thin guiding layer, high efficiency is acquired. Substrate and guiding layer have different bulk shear-horizontal wave speeds [4–6], guiding layer has, by design, a lower wave speed. SAW propagate along $\boldsymbol{e}_1$ direction. On the surface their amplitude are maximum and decay exponentially downward into the substrate in $-\boldsymbol{e}_3$ direction. Love wave propagation is on purpose within a confined guiding layer in order to minimize the attenuation loss [7–9].

On the piezoelectric substrate, Love wave is excited by an InterDigital-Transducer (IDT) array that is composed of a finger arrangement of electrode pins as visualized in the inset of Fig. 1. Half of the fingers are assigned to an alternating potential, $V_\mathrm{f}(t)$ in V, while the others are grounded, $V_\mathrm{g} = 0$. Electrode pairs with different potentials impose indirect piezoelectric effect, which causes mechanical waves to propagate at the surface in time. Biomarkers passing by within convecting fluid are accumulated on a functionalized surface above the guiding layer in a sensing operation [10–12]. Accumulated agents increase the mass that imposes a mechanical perturbation on the surface and shift the resonance frequency due to the change in the Love wave speed [13–15].

Design of an optimized Love wave sensor is considered in this study. Sensor design exploits computational models [16] by using materials response [17–19] as well as structural configuration [20, 21]. Specifically, a bilayer composition is utilized for igniting different mechanisms within the structure [22, 23]. The objective is to achieve the highest mass sensitivity, $S_m^v$ in $\mathrm{cm}^2/\mathrm{g}$, with respect to guiding layer thickness, $h$ in µm. $S_m^v$ is selected as a design criterion because it can directly be related to the dispersive characteristic of the Love waves. Mass sensitivity, $S_m^v$, may be defined in terms of the added mass by resorting to the perturbation theory [24–

✉ Bilen Emek Abali
bilenemek@abali.org

[1] Faculty of Engineering, Yeditepe University, 34755 Atasehir, Istanbul, Turkey

[2] Division of Applied Mechanics, Department of Materials Science and Engineering, Uppsala University, Box 35, 751 03 Uppsala, Sweden

Published online: 10 May 2024

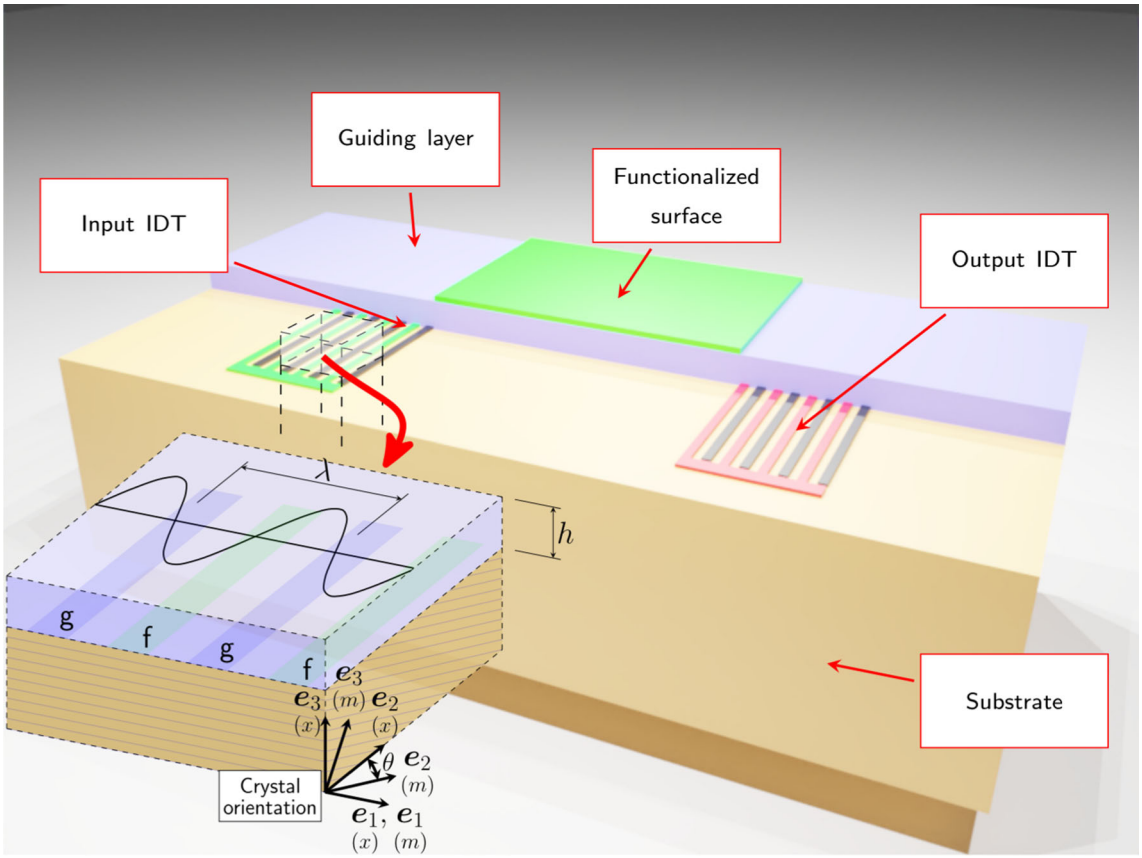


**Fig. 1** Illustration of Love wave mechanics on a section of a two-layered medium, where $(x)$ and $(m)$ are the device (global) and the material coordinate systems, respectively

26]. However, [27] indicates that perturbation theory based calculation deviates from experimental results. Alternatively, [28] also gives $S_m^v$ using the wave speed dispersion curves. Calculation of $S_m^v$ from the dispersion curve performs better such that [29] has presented an explicit calculation of $S_m^v$ from a transient finite element solution for a two-pins-array sensor geometry. Yet, the transient solution has to reach the steady-state response for which time and resource might scale up with respect to the time step duration and mesh resolution. In fact, steady-state wave mode obtained in the transient solution is made up of a number of waves and $S_m^v$ solution for a specific wave mode may not be applicable.

Taking advantage of the dispersion phenomenon in substrate/layer systems, we propose a digital twin of this complex system in order to design computationally the parameters in such a device. We explain and verify the performed guideline based on modal analysis to determine the optimal wave guiding layer thickness, $h$, providing highest mass sensitivity. In this regard, in Sect. 2, we explain the methodology and determine the optimal wave guiding layer thickness. We develop a digital twin of the system with two different approaches. A transient formulation is shown with a minimum amount of assumptions. A modal analysis based formulation is presented that allows a fast solution of the system. Then, in Sect. 3, we verify the prediction capacity of this reduced order model by using the transient formulation. Results are then discussed in Sect. 4 with possible future studies in Sect. 5.

## 2 Digital twin and optimization of parameters

Design of an optimized Love wave sensor is based on the so-called mass sensitivity that is related to the wave speed, $v$, along $\boldsymbol{e}_1$ within the wave guiding layer in Fig. 1. This wave speed, $v$, varies as a function of the following design parameters:

- Substrate material
- Guiding layer material
- Crystallographic cutting plane, $\theta$
- Layer thickness, $h$
- Interdigital electrode spacing, $\lambda/2$

**Table 1** Parameter design space with examples from existing products

| Parameter | Possible choices or interval |
|---|---|
| Substrate material | Lithium niobate ($LiNbO_3$), lithium tantalate ($LiTaO_3$), quartz, etc. [30, 31] |
| Wave guiding layer material | Silica ($SiO_2$), zinc oxide (ZnO), titanium dioxide ($TiO_2$), gold (Au), SU-8 photoresists, polymethylmethacrylate (PMMA), polyimide, polydimethylsiloxane (PDMS) |
| Crystallographic cutting plane, $\theta$ | 64YX ($LiNbO_3$), 41YX ($LiNbO_3$), 36YX ($LiTaO_3$), 90-ST (quartz), etc |
| Interdigital electrode spacing, $\lambda/2$ | wavelength, $\lambda \in [52, 78, 104, 130, 156]$ |
| Layer thickness, $h$ | $h \in [0, \lambda]$ |

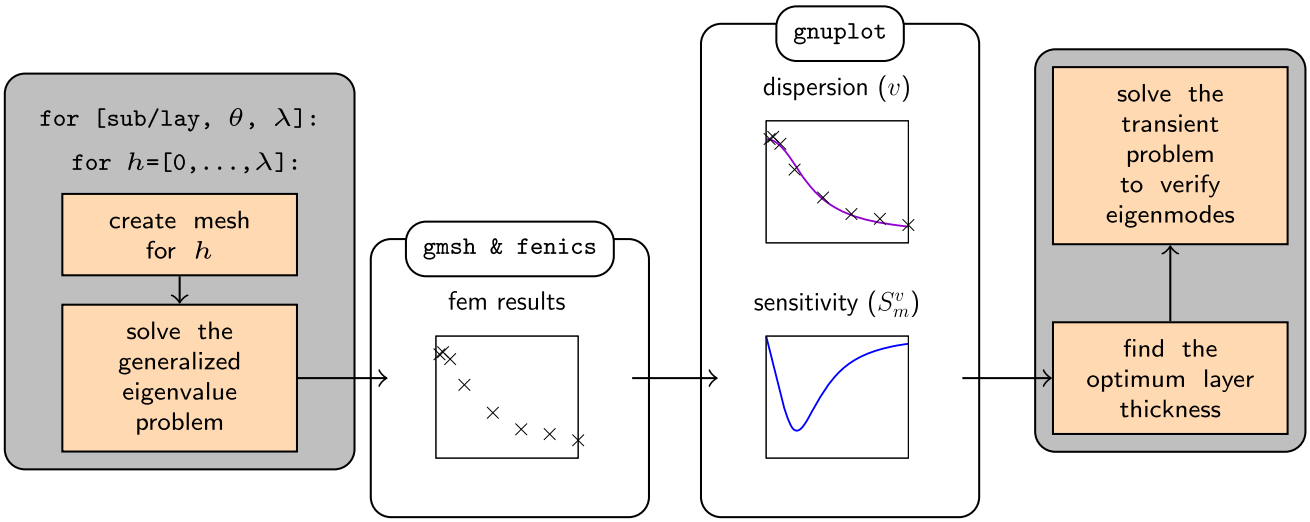


**Fig. 2** Design flowchart to find the optimum layer thickness

In the case of commercial Love wave based transceivers, these parameters may be chosen from a variety of possibilities that we compile the design space in Table 1.

We develop a framework to determine optimal parameters in a design as described in Sect. 2.1. Continuum mechanics based formulation of a sensor design is presented in Sect. 2.2 for acquiring Love wave modes. A reduced order modeling is introduced in Sect. 2.3 in order to obtain a fast digital twin of this complex system. All numerical simulations are computed by the Finite Element Method (FEM). All implementations are utilized with the help of the open-source FEniCS [32].

## 2.1 Design guideline

We propose a design guideline depicted in Fig. 2 that is based on performing a series of numerical simulations within a Representative Volume Element (RVE) while the design parameter $h$ is varied over an appropriate range of values.

The RVE size (length) is set equal to the wavelength, $\lambda$, since the fundamental Love wave mode is $\lambda$-periodic. The RVE and its periodic boundaries are shown in Fig. 3, where the layer thickness, $h$, is varied.

We circumvent ourselves from modeling electrodes between the substrate and the wave guiding layer, as the waves induced by them are generated as an intrinsic property of the RVE. Thus, the Love wave modes appear naturally in the solution to the EigenValue Problem (EVP), because the material configuration provides in-plane particle motion in the vicinity of the free surface. The bottom surface of the substrate is clamped and we perform eigenfrequency calculations for geometries with different layer thicknesses.

Herein we have selected the combination as $LiNbO_3$/silica from the Table 1. The substrate material $LiNbO_3$ is piezoelectric with a lattice structure belonging to trigonal symmetry class, and thus, anisotropic.

Therefore, crystallographic cutting plane, $\theta$, affects the system response significantly. The electro-mechanical coupling is provided by the piezoelectric material behavior and used for creating a wave within the wave guiding layer. The correct choice of $\theta$ makes it possible for Love waves to form. $LiNbO_3$ crystal and its chemical composition are illustrated in Fig. 4 generated by VESTA version 3.5.8 (64-bit). Herein,

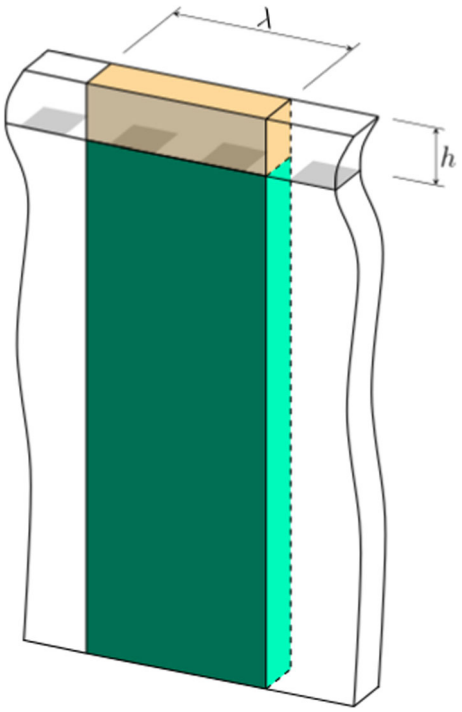


**Fig. 3** SAW sensor's RVE with electrode pins in gray

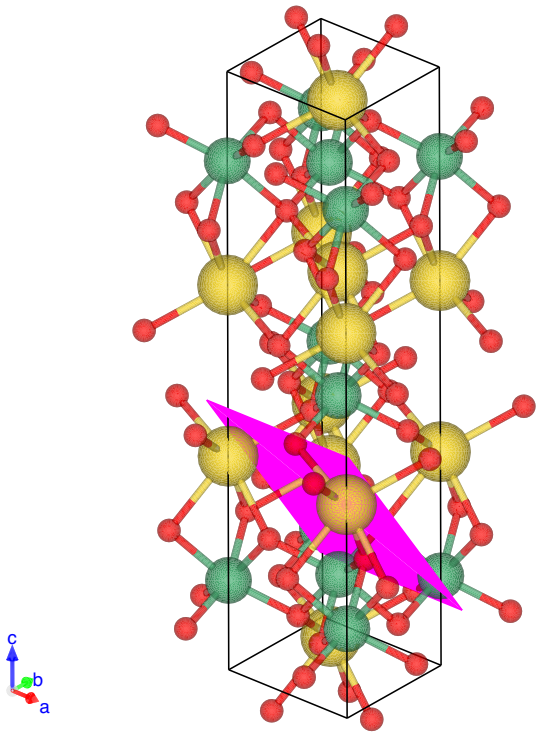


**Fig. 4** Crystal structure of ilmenite type $LiNbO_3$ (Li: yellow, Nb: green, O: red), where the cutting plane is depicted in magenta. The unit cell has coordinates $\boldsymbol{e}_1$, along $\boldsymbol{a}$, in the crystallographic system. The cut resides on the $\underset{(x)}{\boldsymbol{e}_1}$–$\overset{(m)}{\underset{(x)}{\boldsymbol{e}_2}}$ plane. The identifier number of the data used to generate this image is 0019589 that is accessed from American Mineralogist Crystal Structure Database [33]

we use a so-called 64YX-cut configuration that is commonly used in surface acoustic waves transceivers. This nomenclature is specific to piezoelectric materials. For example, a 64YX lithium niobate wafer has the thickness along $y$-axis (the first letter) and is rotated to 64° about $x$-axis (second letter). After this rotation, the crystal is cut into wafers. In other words, the rotation matrix reads

$$\boldsymbol{R} = \begin{pmatrix} 1 & 0 & 0 \\ 0 & \cos(\theta) & -\sin(\theta) \\ 0 & \sin(\theta) & \cos(\theta) \end{pmatrix} \tag{1}$$

between material local coordinates and Cartesian global coordinates.

Interdigital electrode spacing depends on the chosen wavelength, $\lambda$. Herein, we use $\lambda = 104\,\mu\text{m}$ that is caused by manufacturing limitations. Smaller wavelength parameters are possible but seldom used in order to reduce costs. Guiding layer has the thickness of $h$ that is optimized in this study. Technically, it is possible to circumvent a design from using a wave guiding layer, $h = 0$. Since the propagating wave is a surface wave, the maximum thickness is taken as the wavelength, $\lambda$. For growing values of $h$, the wave speed asymptotically converges to the wave guiding layer's shear-horizontal wave speed, and the transition region occurs within a single wavelength.

## 2.2 Electro-mechanical coupling in the finite element method

Alternating voltage is applied, $V_\text{f}(t)$, to the respective electrodes of the IDT while grounding others, $V_\text{g} = 0$. At a given frequency, $f$, a weighted superposition of eigenmodes is expected; yet, the eigenmode closest to $f$ will dominate all other modes. Such an observation is possible by a transient solution of the dynamic problem.

We use standard continuum mechanics notation and understand a summation over repeated indices. Piezoceramics have a coupled phenomenon of mechanics and electricity, we refer to [34, Sect. 3.5] for the complete theory, application examples for small [35] and large [36] deformations. For mechanics, we solve the balance of momentum in order to obtain the displacement, $\boldsymbol{u}$ in m, by satisfying

$$\rho \ddot{u}_i - T_{ji,j} - \rho f_i = F_i \tag{2}$$

where $\dot{()}$ means rate (time derivative); the mass density, $\rho$ in kg/m$^3$, is given; the specific (per mass) body force due to gravity, $\boldsymbol{f}$ in N/kg, is neglected for small devices; and electromagnetic force density (per volume), $\boldsymbol{F}$ in N/m$^3$, vanishes for dielectric (electric insulator) materials. Under these assump-

tions, we model the mechanical stress, $\boldsymbol{T}$ in Pa, in relation with strain, $\boldsymbol{S}$, and electric field, $\boldsymbol{E}$ in V/m, as follows:

$$T_{ij} = C_{ijkl} S_{kl} - e_{kij} E_k \tag{3}$$

for a linear material by using stiffness tensor of rank four, $\boldsymbol{C}$ in Pa, and piezoelectric tensor of rank three, $\boldsymbol{e}$ in Pa V/m. Instead of piezoelectric tensor, the so-called piezoelectric coefficients, $\boldsymbol{d}$ in V/m, are used in the literature, where

$$e_{mij} = C_{ijkl} d_{mkl} \tag{4}$$

The latter is inserted into Eq. (3) and $\boldsymbol{C}$ is factored out,

$$\begin{aligned} T_{ij} &= C_{ijkl} S_{kl} - C_{ijkl} d_{mkl} E_m \,, \\ &= C_{ijkl} (S_{kl} - d_{mkl} E_m) \,, \end{aligned} \tag{5}$$

in order to observe the total infinitesimal linear strain

$$S_{ij} = \frac{1}{2}\left(u_{i,j} + u_{j,i}\right) \tag{6}$$

and the linearized piezoelectric strain, $d_{mkl} E_m$. The comma notation denotes a partial derivative in space. In this manner, it is possible to consider the difference between the total strain, $S_{ij}$, and the piezoelectric strain, $d_{mkl} E_m$, yielding a so-called elastic strain that is in linear relation to stress as known as the Hooke's law. We model a wave propagation in elastic medium, hence, the deformation is small. Therefore, a linear strain measure is used. However, the implementation is generic and linearization is symbolic such that a nonlinear strain measure is possible for incorporating geometric nonlinearities but not necessary for the application herein. The choice of linear material equations is an assumption that is the usual case in the literature for piezoceramics [37–41]. Moreover, use of first order material equations is another assumption. Indeed, higher order material modeling exist [42, 43]; however, such flexoelectric responses are caused by an internal periodic microstructure [44] that is then used to obtain strain gradient parameters [45, 46]. Herein, we use a bulk material without internal substructure such that higher order in strain may be neglected. A crucial assumption is the reversible process because of low Q-impendance of this device. In other words, we neglect any dissipative mechanisms in modeling, otherwise, frequency sweep measurements and material parameters are needed for deformation and polarization [47, 48].

In order to obtain the electric field, we begin with the Gauß's law

$$D_{i,i} = 0 \tag{7}$$

where the charge potential, $\boldsymbol{D}$ in C/m$^2$, reads

$$D_i = e_{ikl} S_{kl} + \varepsilon_{ik} E_k \tag{8}$$

with permittivity, $\varepsilon_{ik}$. By using Voigt notation, we may write the rank three and four tensors of material coefficients as,

$$\boldsymbol{C} = \begin{pmatrix} C_{1111} & C_{1122} & C_{1133} & C_{1123} & C_{1113} & C_{1112} \\ C_{2211} & C_{2222} & C_{2233} & C_{2223} & C_{2213} & C_{2212} \\ C_{3311} & C_{3322} & C_{3333} & C_{3323} & C_{3313} & C_{3312} \\ C_{2311} & C_{2322} & C_{2333} & C_{2323} & C_{2313} & C_{2312} \\ C_{1311} & C_{1322} & C_{1333} & C_{1323} & C_{1313} & C_{1312} \\ C_{1211} & C_{1222} & C_{1233} & C_{1223} & C_{1213} & C_{1212} \end{pmatrix}$$

$$\boldsymbol{d} = \begin{pmatrix} d_{111} & d_{122} & d_{133} & d_{123} & d_{131} & d_{112} \\ d_{211} & d_{222} & d_{233} & d_{223} & d_{231} & d_{212} \\ d_{311} & d_{322} & d_{333} & d_{323} & d_{331} & d_{312} \end{pmatrix}. \tag{9}$$

No external magnetic flux is applied and all materials are non-conductive such that no magnetic flux is induced. Hence, we neglect the magnetic flux and the electric field is then given as

$$E_i = -\phi_{,i} \tag{10}$$

where an electric potential, $\phi$ in V, is the unknown to be computed from the Gauß's law in Eq. (7).

Governing Eqs. (2) and (7) are rewritten in a so-called weak form by multiplying Eqs. (2), (7) by appropriate test functions, $\delta\boldsymbol{u}$ in m, $\delta\phi$ in V$\hat{=}$J/C, leading to integral forms in J,

$$\begin{aligned} &\int_\Omega \left(\rho \ddot{u}_i - T_{ji,j}\right) \delta u_i \, \mathrm{d}V = 0, \\ &-\int_\Omega D_{i,i} \delta\phi \, \mathrm{d}V = 0. \end{aligned} \tag{11}$$

For a discrete representation, we use a mixed space formulation such that the unknowns, $\phi$, $\boldsymbol{u}$, are solved at once instead of a staggered approach. This monolithic solution method ensures that the electro-mechanical coupling is captured at the accuracy of the solver tolerances. We employ a discretization using Lagrange elements and generate piecewise continuous polynomials that are adequate for approximation in $\mathcal{H}_0$. This triangulation is denoted $\mathcal{T}$ and consists of non-overlapping triangles, $\tau$. We use linear elements, $\mathcal{P}_1$, with a polynomial degree 1 for all unknowns. As known as the Galerkin approach, we use the same space for trial and test functions, thus, four unknowns, $\phi, u_1, u_2, u_3$, construct a mixed space of a scalar and vector in 3-D as a discrete representation of the continuum

$$\begin{aligned} \mathcal{V} = \Big\{ &\left\{\phi\right\} \in \left[\mathcal{H}_0(\Omega)\right]^1 : \left\{\phi\right\}\Big|_\tau \in \mathcal{P}_1(\tau) \; \forall \tau \in \mathcal{T} \\ &\wedge \left\{u_i\right\} \in \left[\mathcal{H}_0(\Omega)\right]^3 : \left\{u_i\right\}\Big|_\tau \in \mathcal{P}_1(\tau) \; \forall \tau \in \mathcal{T} \Big\}. \end{aligned} \tag{12}$$

In connection with this choice, we utilize an integration by parts, for obtaining the following weak forms that are well defined in the aforementioned space

$$\begin{aligned}\text{Form}_{\boldsymbol{u}} &= \int_\Omega \left(\rho \ddot{u}_i \delta u_i + T_{ji}\delta u_{i,j}\right) \mathrm{d}V \\ &\quad - \int_{\partial\Omega} n_j T_{ji} \delta u_i \,\mathrm{d}A = 0\,, \\ \text{Form}_{\phi} &= \int_\Omega D_i \delta\phi_{,i}\,\mathrm{d}V - \int_{\partial\Omega} n_i D_i \delta\phi \,\mathrm{d}A = 0\,. \end{aligned} \tag{13}$$

On internal boundaries, boundary integrals cancel out because of jump conditions. For a field, $\alpha$, we may introduce jump brackets, $[\![\alpha]\!] = \alpha^+ - \alpha^-$, indicating the difference between $\alpha$ value calculated by shape functions of one element and neighboring element. In the case of displacements, stress projected along the surface normal is the same on neighboring elements, $n_j[\![T_{ji}]\!] = 0$, which is also called Newton's second lemma or "actio" equals "reactio." In the case of charge potential the jump vanishes as a result of Maxwell equations, $n_i[\![D_i]\!] = 0$, since there are no surface charges in internal boundaries. For the boundaries of the outer surface, we must define boundary conditions. On the bottom and top surfaces we assume, $n_j\sigma_{ji} = 0$, and electric isolation, $n_i D_i = 0$, such that we obtain

$$\begin{aligned}\text{Form} &= \text{Form}_{\boldsymbol{u}} + \text{Form}_{\phi} = 0 \\ \text{Form} &= \int_\Omega \left(\rho \ddot{u}_i \delta u_i + T_{ji}\delta u_{i,j} + D_i \delta\phi_{,i}\right) \mathrm{d}V\,, \end{aligned} \tag{14}$$

where we stress that the forms have the same unit. Inserting Eqs. (6) and (10) into the latter, we obtain

$$\begin{aligned}\text{Form} = \int_\Omega &\left(\rho\delta u_i \ddot{u}_i + \delta u_{i,j} C_{jikl} S_{kl}\right. \\ &\left. - \delta u_{i,j} e_{kji} E_k + \delta\phi_{,i} e_{ikl} S_{kl} + \delta\phi_{,i}\varepsilon_{ik} E_k\right) \mathrm{d}V\,. \end{aligned} \tag{15}$$

Solving the weak form by equating it to zero delivers $\boldsymbol{u}$ and $\phi$.

We use a time and space discretization for solving Eq. (15). For time discretization, a finite difference method is employed by the Euler backward scheme with a constant time step

$$\Delta t = \frac{1}{f n_t} \tag{16}$$

where $f$ is the frequency and $n_t$ is the number of time steps in one period. The weak form reads

$$\begin{aligned}\text{Form}_{\Delta t} = \int_\Omega &\left(\rho\delta u_i \frac{u_i - 2u_i^0 + u_i^{00}}{\Delta t^2} + \delta u_{i,j} C_{jikl} S_{kl}\right. \\ &\left. - \delta u_{i,j} e_{kji} E_k + \delta\phi_{,i} e_{ikl} S_{kl} + \delta\phi_{,i}\varepsilon_{ik} E_k\right) \mathrm{d}V \end{aligned} \tag{17}$$

where $^0$ and $^{00}$ superscripts represent previous time steps in increasing order.

### 2.3 Generalized eigenvalue problem

We create an eigenvalue problem and search the Love modes around intrinsic SAW phase speeds of the two layered system. Yet the solution of this eigenvalue problem proves to create a computational challenge as the second time derivative of displacement brings the so-called mass terms in $\text{Form}_u$, while no such terms exists in $\text{Form}_\phi$. Thus, the deficiency is in mass terms and a possible solution relies on a method known as static condensation [49, 50]. In this approach, the problem is reformulated in such a way that the electric potential degrees of freedom are replaced.

Formulating the problem as a first-order system allows rewriting the equations of motion by decomposing space and time dependencies using the Bernoulli separation ansatz as follows:

$$\begin{aligned} u_j(x,t) &= u_j(x)\exp(-\mathrm{i}\omega t)\,, \\ \phi(x,t) &= \phi(x)\exp(-\mathrm{i}\omega t)\,, \end{aligned} \tag{18}$$

where $\omega$ is the monotonic frequency of excitation in rad/s, and the exponential function that collects sinus and cosinus responses in time, such that the second order terms reduce to $\ddot{u}_j = -\omega^2 u_j$. For each unknown in the form functionals, we select test and trial functions from the same function space, as in the Galerkin approach. As usual, we approximate the fields by using shape functions, $N_i$ and $N$, as vector and scalar depending only on space,

$$\begin{aligned} u_i &= \sum_{\mathrm{ID}}^{3n} N_i^{\mathrm{ID}} \hat{u}^{\mathrm{ID}} \quad \delta u_i = \sum_{\mathrm{ID}}^{3n} N_i^{\mathrm{ID}} \mathbf{1}^{\mathrm{ID}} \\ \phi &= \sum_{\mathrm{ID}}^{n} N^{\mathrm{ID}} \hat{\phi}^{\mathrm{ID}} \quad \delta\phi = \sum_{\mathrm{ID}}^{n} N^{\mathrm{ID}} \mathbf{1}^{\mathrm{ID}} \end{aligned} \tag{19}$$

where $n$ is the number of mesh nodes. In this way, as we sum up over elements, denoted by $\sum_e$, and obtain $\hat{\boldsymbol{u}}$ and $\hat{\boldsymbol{\phi}}$ as arrays of the nodal values within the computational domain, the first expression within the integrand in Eq. (15) is assembled as the mass matrix,

$$
\begin{aligned}
\boldsymbol{\delta u}^T \cdot \boldsymbol{K}_{uu} \cdot \boldsymbol{u} &= \sum_e \int_V \delta u_{j,i} C_{ijkl} S_{kl} \, \mathrm{d}V \\
&= \left( \sum_e \int_{\Omega^e} N^{\mathrm{ID}}_{j,i} C_{ijkl} N^{\mathrm{ID}}_{k,l} \, \mathrm{d}V \right) \hat{u}^{\mathrm{ID}} \\
\boldsymbol{\delta u}^T \cdot \boldsymbol{K}_{u\phi} \cdot \boldsymbol{\phi} &= -\sum_e \int_V \delta u_{j,i} e_{kij} E_k \, \mathrm{d}V \\
&= \left( \sum_e \int_{\Omega^e} N^{\mathrm{ID}}_{j,i} e_{kij} N^{\mathrm{ID}}_{,k} \, \mathrm{d}V \right) \hat{\phi}^{\mathrm{ID}} \\
\boldsymbol{\delta \phi}^T \cdot \boldsymbol{K}_{\phi u} \cdot \boldsymbol{u} &= \sum_e \int_V \delta \phi_{,i} e_{ikl} S_{kl} \, \mathrm{d}V \\
&= \left( \sum_e \int_{\Omega^e} N^{\mathrm{ID}}_{,i} e_{ikl} N^{\mathrm{ID}}_{k,l} \, \mathrm{d}V \right) \hat{u}^{\mathrm{ID}} \\
\boldsymbol{\delta \phi}^T \cdot \boldsymbol{K}_{\phi\phi} \cdot \boldsymbol{\phi} &= \sum_e \int_V \delta \phi_{,i} \varepsilon_{ik} E_k \, \mathrm{d}V \\
&= \left( \sum_e \int_{\Omega^e} N^{\mathrm{ID}}_{,i} \varepsilon_{ik} N^{\mathrm{ID}}_{,k} \, \mathrm{d}V \right) \hat{\phi}^{\mathrm{ID}} \\
\boldsymbol{\delta u}^T \cdot \boldsymbol{M} \cdot \boldsymbol{u} &= -\sum_e \omega^2 \int_V \rho \delta u_j u_j \, \mathrm{d}V \\
&= \left( -\sum_e \omega^2 \int_{\Omega^e} \rho N^{\mathrm{ID}}_j N^{\mathrm{ID}}_j \, \mathrm{d}V \right) \hat{u}^{\mathrm{ID}} \qquad (20)
\end{aligned}
$$

By observing Eq. (20)$_{2,3}$, we realize that $\boldsymbol{K}_{\phi u}$ is the transpose of $\boldsymbol{K}_{u\phi}$. Now, we rewrite in the matrix form

$$
\left( \begin{pmatrix} \boldsymbol{K}_{uu} & \boldsymbol{K}_{u\phi} \\ \boldsymbol{K}^{\mathsf{T}}_{u\phi} & \boldsymbol{K}_{\phi\phi} \end{pmatrix} - \omega^2 \begin{pmatrix} \boldsymbol{M} & \boldsymbol{0} \\ \boldsymbol{0} & \boldsymbol{0} \end{pmatrix} \right) \begin{Bmatrix} \hat{\boldsymbol{u}} \\ \hat{\boldsymbol{\phi}} \end{Bmatrix} = 0 \, . \qquad (21)
$$

The second line is observed as

$$
\boldsymbol{K}^{\mathsf{T}}_{u\phi} \cdot \hat{\boldsymbol{u}} + \boldsymbol{K}_{\phi\phi} \cdot \hat{\boldsymbol{\phi}} = 0 \qquad (22)
$$

which is used to solve for $\hat{\boldsymbol{\phi}} = -\boldsymbol{K}^{-1}_{\phi\phi} \cdot \boldsymbol{K}^{\mathsf{T}}_{u\phi} \cdot \hat{\boldsymbol{u}}$. By inserting this into the first row of Eq. (21), we acquire

$$
\boldsymbol{K}_{uu} \cdot \hat{\boldsymbol{u}} - \boldsymbol{K}_{u\phi} \cdot \boldsymbol{K}^{-1}_{\phi\phi} \cdot \boldsymbol{K}^{\mathsf{T}}_{u\phi} \cdot \hat{\boldsymbol{u}} - \omega^2 \boldsymbol{M} \cdot \hat{\boldsymbol{u}} = 0. \qquad (23)
$$

By collecting the coefficients of $\hat{\boldsymbol{u}}$ from the first two terms we arrive at the condensed stiffness matrix, written as

$$
\boldsymbol{K}^* = \boldsymbol{K}_{uu} - \boldsymbol{K}_{u\phi} \cdot \boldsymbol{K}^{-1}_{\phi\phi} \cdot \boldsymbol{K}^{\mathsf{T}}_{u\phi}. \qquad (24)
$$

Substituting this back into Eq. (23), we arrive at the simplified form of the generalized eigenvalue problem having two Hermitian (equivalent to symmetric since all entries are real numbers) non-identity matrices, while $\boldsymbol{M}$ shall be a positive definite matrix [51].

$$
(\boldsymbol{K}^* - \omega^2 \boldsymbol{M}) \hat{\boldsymbol{u}} = 0. \qquad (25)
$$

The corresponding eigenvectors, or the modeshapes, to the calculated eigenvalues, $\omega^2$, are the displacements, $\hat{\boldsymbol{u}}$.

SLEPc provides iterative methods such as ARPACK [52] to solve the eigenvalues of large matrices more efficiently. We utilize spectral transform in order to specify a target eigenvalue, $\sigma$, around which a number of eigenvalues, $n_{\mathrm{eig}}$, are solved [53]. The target eigenvalue, $\sigma$, is determined after calculating the bulk shear-horizontal wave speed in the materials on $x_1 x_2$ plane.

$$
v_b = \sqrt{\frac{C_{1212}}{\rho}}. \qquad (26)
$$

Selection of $\sigma$ should be experimented after execution of the solver. But, a rule of thumb is to choose $v_b$ as $v_s$ if $\bar{h}$ is less than or equal to 0.5, else as $v_g$, such that

$$
\sigma = \left( \frac{2\pi v_b}{\lambda} \right)^2, \qquad (27)
$$

while keeping $n_{\mathrm{eig}}$ at 30 that one may get enough range of eigenvectors to visually assess the Love mode. After ascertaining the mode and therefore its eigenvalue, $\omega_i^2$, we find

$$
v_i = \lambda \frac{\omega_i}{2\pi}, \qquad (28)
$$

and thus the resulting operating frequency, $f$, shall be

$$
f_i = \frac{v_i}{\lambda}. \qquad (29)
$$

### 2.4 Thickness optimization

For each wave guiding layer thicknesses in Table 2, a mesh is prepared and used in FEniCS in order to solve the corresponding generalized eigenvalue problem. Eigenvalues have been converted into wave speeds and then used for fitting by the mass sensitivity function in Eq. (40). The optimal wave guiding layer thickness is expected at the minimum value of the mass sensitivity curve.

The computational domain is composed of a substrate and a wave guiding layer. We emphasize that the substrate material is anisotropic such that we differentiate between the material coordinate system denoted by $(m)$ and global coordinate system for the simulation denoted by $(x)$. We define material parameters of the substrate $\left( \underset{(m)}{\boldsymbol{C}}^{\mathrm{sub}}, \underset{(m)}{\boldsymbol{e}}^{\mathrm{sub}}, \underset{(m)}{\boldsymbol{\varepsilon}}^{\mathrm{sub}}, \rho^{\mathrm{sub}} \right)$ and the wave guiding layer $\left( \underset{(m)}{\boldsymbol{C}}^{\mathrm{lay}}, \underset{(m)}{\boldsymbol{e}}^{\mathrm{lay}}, \underset{(m)}{\boldsymbol{\varepsilon}}^{\mathrm{lay}}, \rho^{\mathrm{lay}} \right)$ as given in Eq. (30). The lithium niobate material is anisotropic with the aforementioned crystal structure in Fig. 4, hence, we obtain from [54] the following values presented in Voigt notation

$$\underset{(m)}{\boldsymbol{C}}^{\text{sub}} = \begin{pmatrix} 198.86 & 54.67 & 67.99 & 7.83 & 0 & 0 \\ 54.67 & 198.86 & 67.99 & -7.83 & 0 & 0 \\ 67.99 & 67.99 & 234.18 & 0 & 0 & 0 \\ 7.83 & -7.83 & 0 & 59.85 & 0 & 0 \\ 0 & 0 & 0 & 0 & 59.85 & 7.83 \\ 0 & 0 & 0 & 0 & 7.83 & 720.9 \end{pmatrix} \times 10^{-3}\ \text{TPa} \tag{30}$$

$$\underset{(m)}{\boldsymbol{e}}^{\text{sub}} = \begin{pmatrix} 0 & 0 & 0 & 0 & 3.655 & 0 \\ -2.407 & 2.407 & 0 & 3.655 & 0 & 0 \\ 0.328 & 0.328 & 1.894 & 0 & 0 & 0 \end{pmatrix} \times 10^{-6}\mu\text{C}/\mu\text{m}^2$$

$$\underset{(m)}{\boldsymbol{\varepsilon}}^{\text{sub}} = \begin{pmatrix} 44.9 & 0 & 0 \\ 0 & 44.9 & 0 \\ 0 & 0 & 26.7 \end{pmatrix} \tag{31}$$

$$\rho_{\text{sub}} = 4642.8 \times 10^{-12}\ \text{mg}/\mu\text{m}^3 \tag{32}$$

For the isotropic $SiO_2$ wave guiding layer the following properties [55] have been used.

$$\underset{(m)}{\boldsymbol{C}}^{\text{lay}} = \begin{pmatrix} 70.94 & 14.53 & 14.53 & 0 & 0 & 0 \\ 14.53 & 70.94 & 14.53 & 0 & 0 & 0 \\ 14.53 & 14.53 & 70.94 & 0 & 0 & 0 \\ 0 & 0 & 0 & 28.21 & 0 & 0 \\ 0 & 0 & 0 & 0 & 28.21 & 0 \\ 0 & 0 & 0 & 0 & 0 & 28.21 \end{pmatrix} \times 10^{-3}\ \text{TPa} \tag{33}$$

$$\underset{(m)}{\boldsymbol{e}}^{\text{lay}} = 0\ \text{C}/\mu\text{m}^2$$

$$\underset{(m)}{\boldsymbol{\varepsilon}}^{\text{lay}} = \begin{pmatrix} 3.8 & 0 & 0 \\ 0 & 3.8 & 0 \\ 0 & 0 & 3.8 \end{pmatrix} \tag{34}$$

$$\rho_{\text{lay}} = 2196.0 \times 10^{-12}\ \text{mg}/\mu\text{m}^3 \tag{35}$$

Love waves have been acquired by rotating the material coordinates to global coordinates by using the transformation matrix,

$$\boldsymbol{Q} = \boldsymbol{R}^T = \begin{pmatrix} 1 & 0 & 0 \\ 0 & \cos(\varphi) & \sin(\varphi) \\ 0 & -\sin(\varphi) & \cos(\varphi) \end{pmatrix}. \tag{36}$$

This transformation is in line with the YX-cut 64° such that a rotation around $x$-axis is performed first. Then a subsequent rotation is performed around $x$-axis by −90° in order to align the thickness direction with $z$-axis in the simulation.

By using the coordinate transformation, we obtain

$$\begin{aligned} \underset{(x)}{C}^{\text{sub}}_{ijkl} &= Q_{ai} Q_{bj} Q_{ck} Q_{dl}\, \underset{(m)}{C}^{\text{sub}}_{abcd}, \\ \underset{(x)}{e}^{\text{sub}}_{ijk} &= Q_{ai} Q_{bj} Q_{ck}\, \underset{(m)}{e}^{\text{sub}}_{abc}, \\ \underset{(x)}{\varepsilon}^{\text{sub}}_{ij} &= Q_{ai} Q_{bj}\, \underset{(m)}{\varepsilon}^{\text{sub}}_{ab} \end{aligned} \tag{37}$$

The meshes in Fig. 5 (prepared in Gmsh, [56]) correspond to the RVE model in Fig. 3 utilizing the thicknesses provided in Table 2. The substrate dimensions in the $\underset{(x)}{\boldsymbol{e}}_1$, $\underset{(x)}{\boldsymbol{e}}_2$, and $\underset{(x)}{\boldsymbol{e}}_3$ directions are equal to 104 μm, 20 μm, and 700 μm, respectively. Periodic boundary conditions have been applied over adjacent planes normal to $\underset{(x)}{\boldsymbol{e}}_1$ and $\underset{(x)}{\boldsymbol{e}}_2$ directions. Identical face meshing is applied on each periodic face pair. The electrical potential, $\phi$ as well as displacement, $u_i$, degrees of freedom are linked periodically across the appropriate face pairs.

Each line in Eq. (20) is assembled in matrices and then converted to $\boldsymbol{M}$ and $\boldsymbol{K}^*$ as in Eq. (24). $\boldsymbol{M}$, and $\boldsymbol{K}^*$ are Hermitian matrices due to the fact that they are equal to their conjugate transpose. A spectral transform algorithm is applied in order to solve for a group of 30 modes ($\omega^2$ values) in the vicinity of $\sigma$ using the ARPACK solver.

We select the $\omega^2$ values associated with the mode shape corresponding to the Love wave modes. These values may be converted to $v$ by Eq. (28) and are presented in the second row of Table 2 as well as depicted in Fig. 5. In the literature, a relation of wave guiding layer's thickness to frequency (or wave speed) is often called a dispersion equation [29, 57, 58] that is also expressed in a closed form solution after the following assumptions:

- Kinematics of the surface wave has been assumed to show surface-transverse particle displacements.
- A wave propagation in $\underset{(x)}{\boldsymbol{e}}_1$ direction.
- Continuous displacements at the interface of two materials.
- The substrate and the wave guiding layer are both isotropic.

For presenting the result in the used notation herein, we normalize the layer thickness with respect to the wavelength,

$$\bar{h} = \frac{h}{\lambda}. \tag{38}$$

In addition, a constant, $\alpha$, is introduced as the moduli ratio of the material system,

$$\alpha = \frac{\mu_s}{\mu_g} \tag{39}$$

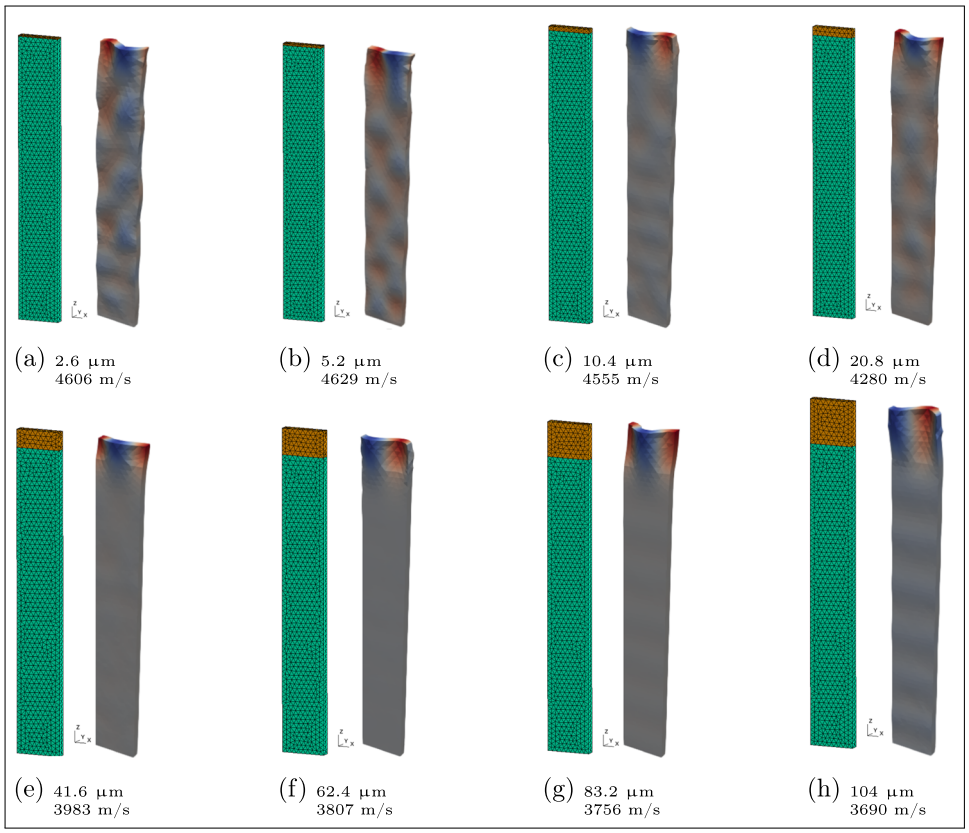


**Fig. 5** Meshes, $v$, and $\hat{\boldsymbol{u}}$ obtained for different $h$

**Table 2** Each mesh is created for a wave guiding layer thickness given in the first row. Solution is from the generalized eigenvalue problem with the resulting Love wave speeds

| $h$ (μm) | 2.6 | 5.2 | 10.4 | 20.8 | 41.6 | 62.4 | 83.2 | 104 |
|---|---|---|---|---|---|---|---|---|
| $v$ (m/s) | 4605 | 4629 | 4555 | 4280 | 3983 | 3807 | 3756 | 3690 |

where $\mu_s$ and $\mu_g$ (in Pa) denote the shear moduli of the substrate and the wave guiding layer, respectively. After some straightforward mathematical manipulations, the dispersion equation reads in terms of the above parameters as:

$$\bar{h} = \frac{1}{2\pi\sqrt{v^2/v_g^2 - 1}} \arctan\left(\alpha \sqrt{\frac{1 - v^2/v_s^2}{v^2/v_g^2 - 1}}\right) \tag{40}$$

where $v_s$, and $v_g$ are the bulk shear-horizontal wave speeds in the substrate and the wave guiding layer (in m/s), respectively. The mass sensitivity, $S_m^f$, is defined as

$$S_m^f = \frac{1}{\rho_g f_s} \frac{\partial f}{\partial \bar{h}} \tag{41}$$

where $f$ is the frequency of the surface wave, $\rho_g$ is the density of the wave guiding layer, and $f_s$ is the frequency of the bulk shear-horizontal wave of the substrate. Since the wave speed will be used in plotting wave dispersion curves instead of the resonance frequency, we rewrite Eq. (41) in terms of $v$ as

$$S_m^v = \frac{1}{v_s} \frac{1}{\lambda \rho_g} \frac{\partial v}{\partial \bar{h}}. \tag{42}$$

Finally, we postulate that the mass sensitivity is the highest at a layer thickness

$$h^* = \operatorname{argmin}\left(\frac{1}{v_s \lambda \rho_g} \frac{\partial v}{\partial \bar{h}}\right). \tag{43}$$

Equation (43) is different from the mass sensitivity solution that uses perturbation theory mentioned in [24, 29, 57].

Under the aforementioned simplifications, Eq. (40) is representing the dispersion relation. Herein, we have used an eigenvalue solution by circumventing many of these assumptions, hence, we expect a more accurate relation. However, the functional form is probably related to the obtained numerical solution. Hence, we use Eq. (40) as a fit function with parameters, $\alpha$, $v_s$, $v_g$ to determine. Initial condition for $\alpha$ are calculated as

**Table 3** Difference between the values supplied as material parameters, $\alpha$ from Eq. (44), $v_s$ from [30], and $v_g$ from Eq. (45), and those obtained from the fit

| Parameter | Initial values | Fit values | Difference (%) |
|---|---|---|---|
| $\alpha$ | 2.30167 | 2.32484 | 1.01 |
| $v_s$ (m/s) | 4712.0 | 4609.8 | 2.17 |
| $v_g$ (m/s) | 3629.0 | 3603.7 | 0.70 |

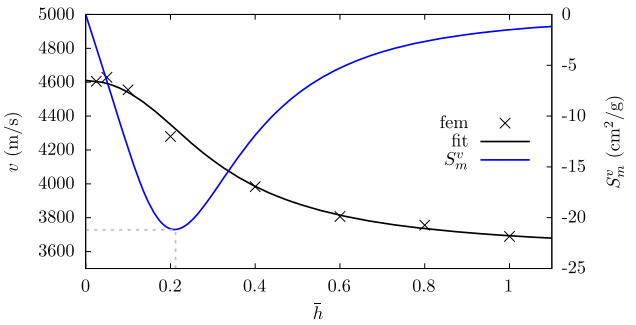


**Fig. 6** Plot of fitted Eq. (40) on the computed $v$ from the eigenvalue problem of Eq. (25)

$$\alpha_0 = \frac{C^{\text{sub}}_{(x)1212}}{C^{\text{lay}}_{(x)1212}} = \frac{64.92 \times 10^{-3}\ \text{TPa}}{28.92 \times 10^{-3}\ \text{TPa}} = 2.30167, \tag{44}$$

while the initial condition for the SAW speed for an open circuit configuration, $v_s$, has been taken as 4712 m/s according to [30]. Finally, the initial condition for $v_g$ is calculated using

$$v_{g0} = \sqrt{\frac{\mu_g}{\rho_g}} = \sqrt{\frac{28.92 \times 10^{-3}\ \text{TPa}}{2196 \times 10^{-12}\ \text{mg}/\mu\text{m}^3}} = 3628.97\ . \tag{45}$$

The initial values and fitted values are tabulated with their asymptotic standard error (ASE) in Table 3.

For demonstrating the quality of the fit, we plot the numerical values and obtained fit curve in Fig. 6. The sensitivity $S_m^v$ from Eq. (42) has been plotted on the same figure as well.

Minimum of the $S_m^v$ is equal to $-21.158\,\text{cm}^2/\text{g}$, which is obtained at $h^* = 21.96\,\mu\text{m}$. The wave velocity at $h^*$ is implicitly solved by Eq. (40), and determined as 4325 m/s. $f^*$ is equal to 41.59 MHz, which is solved by Eq. (29). We verify the wave mode by an additional transient solution for the same RVE in what follows.

## 3 Verification of the numerical solution

We have performed a digital twin by a reduced order system and an optimization procedure in order to obtain the wave guiding layer's thickness. Two additional simulations are conducted in order to verify the assumed Love mode and functionality of the device, as follows:

- Verifying the assumed Love mode by a transient solution of the RVE
- Verifying the working principle of the IDT device as a full sensor model

In order to verify the assume Love mode, a transient solution has been solved for the unit cell geometry with the optimal guiding layer of 21.96 µm thickness. The computational domain has 3936 DOFs. The waves are excited by applying a sinusoidal electric potential at the corresponding frequency of 41.59 MHz determined in the last section. The electric potential is applied on the gray patches visible in Fig. 3. At a point on the electrode, the displacement response of the unit cell is shown in Fig. 7, which is a shear dominated wave in the $x_1$ $x_2$-plane. Propagating along $x_1$ direction, a Love wave mode is visible since $u_2$ is larger than $u_1$ and $u_3$. Still, there is a significant contribution of $u_1$ and $u_3$ such that there is a mixture of thickness shear and twist modes.

In order to verify the working principle of the IDT arrangement, a Direct Numerical Simulation (DNS) of the full sensor has been realized. In this way, we verify the taken assumptions' significance to the output. The whole application is visualized in Fig. 1 and the full sensor model is composed of a substrate, wave guiding layer, interdigital transducer (IDT) as different materials. The IDT array has a well-established finger arrangement to generate and detect waves in a three-dimensional geometry as shown in Fig. 8 designed in SALOME v9.9 [59]. As the generated acoustic wave's shape and propagation is effected by piezoelectric cut (material orientation) and chosen vibration frequency, we perform a direct numerical study with the domain in Fig. 8 consisting of 4 802 636 DOFs. The wave guiding layer is of height 21.96 µm. The IDTs are made of brass, modeled as a linear, isotropic and elastic solid. The displacement at the bottom plane are fixed using Dirichlet boundary condition. A sinusoidal electric potential input is given at the interface between the floating input electrodes and the substrate at a frequency of 41.59 MHz that is the optimized guiding layer determined in the last section.

The DNS of the full sensor results in displacement and electric voltage distribution for a period divided by 50 time steps in order to capture the detailed change over time. For a time instant at 700th time step corresponding to 0.337 µs, we visualize the solution in Fig. 9, where the electric potential vanishes and rate of displacement is maximum creating

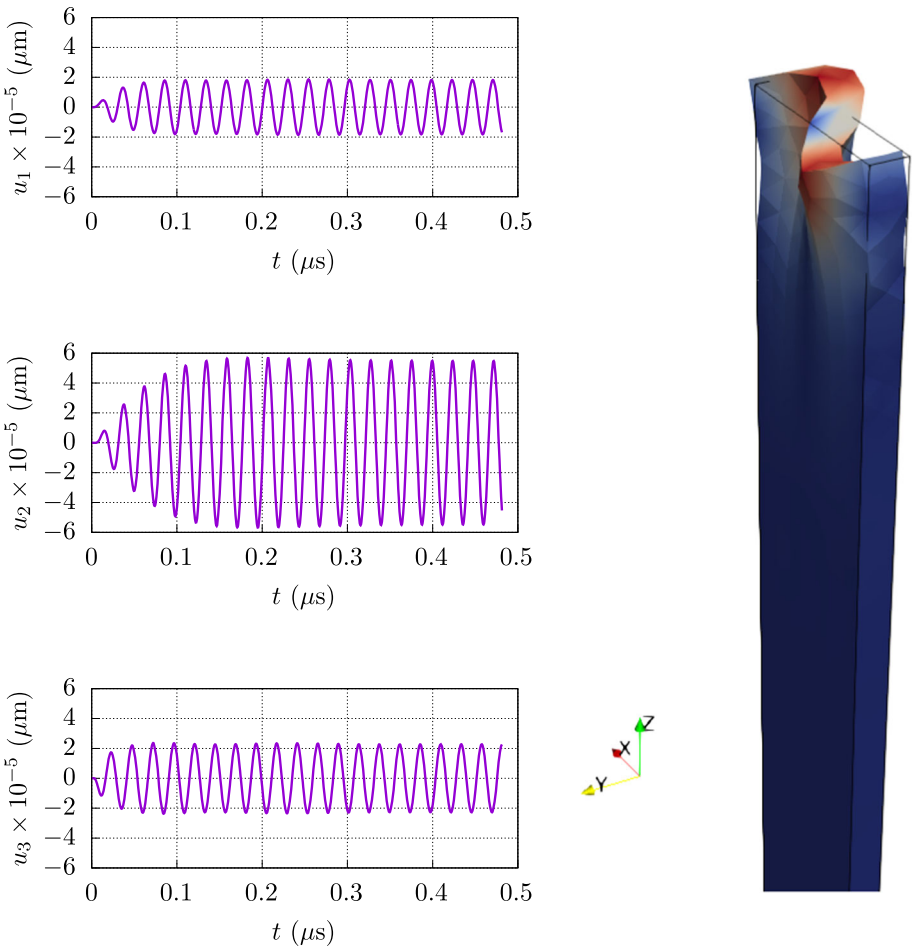


**Fig. 7** Displacement-time history is monitored at 0.204 μs at a point on the free-surface of the RVE having the optimized thickness

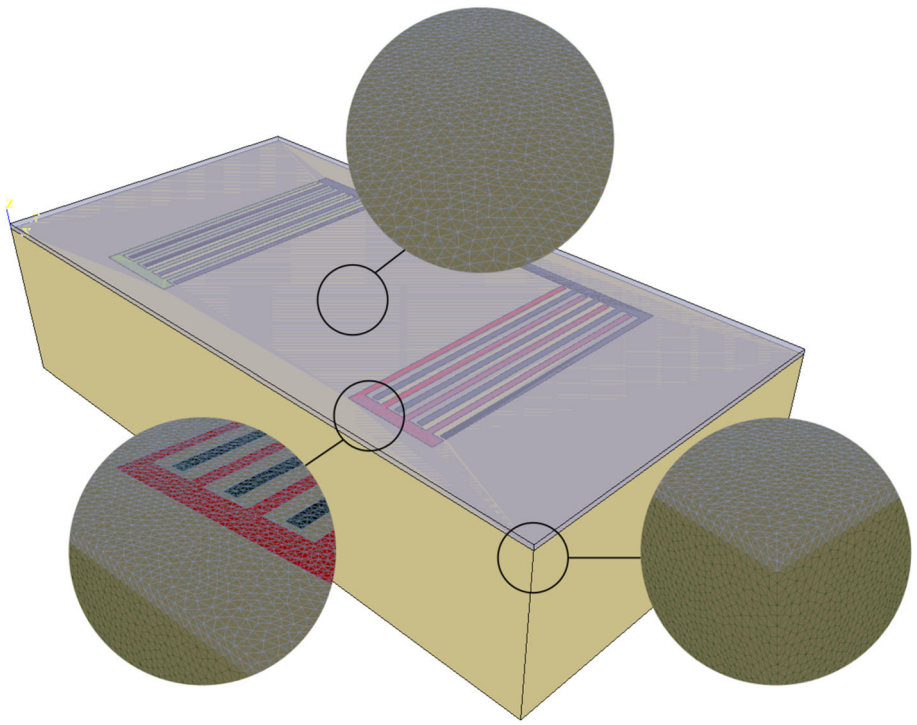

**Fig. 8** Full sensor geometry used in the transient solution

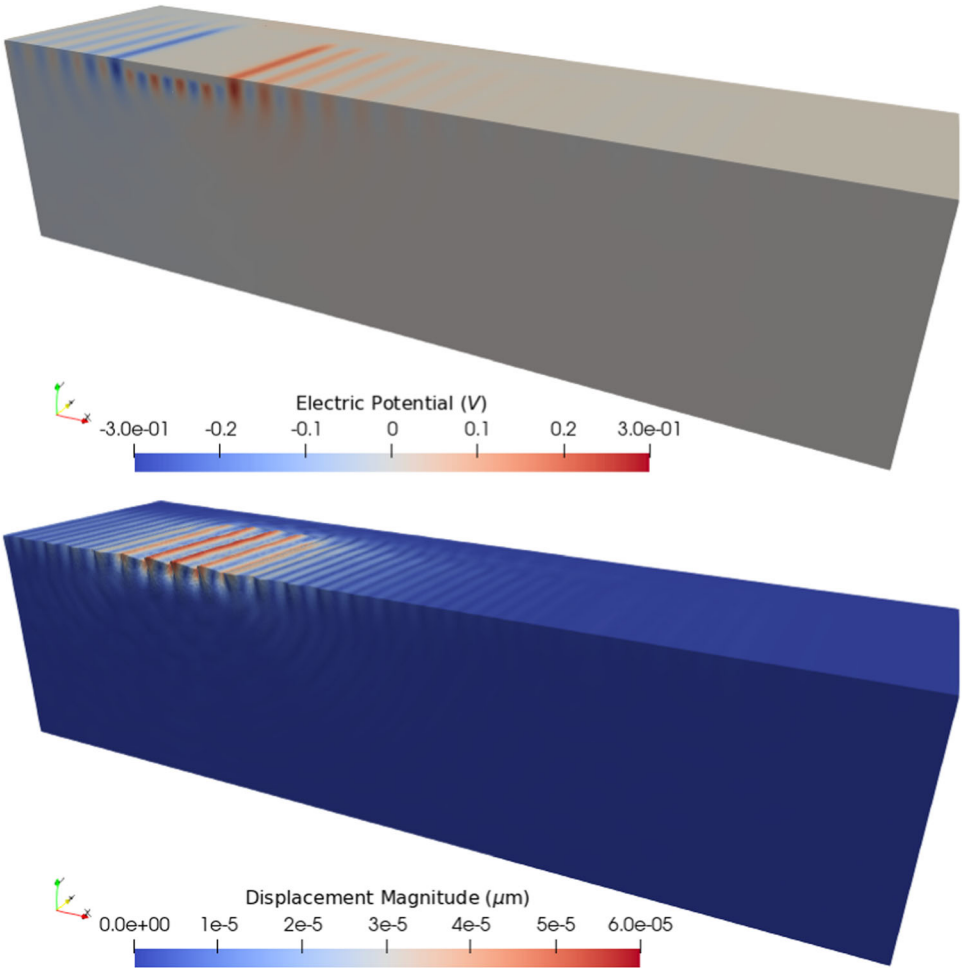


**Fig. 9** Solution at $t = 0.337$ μs, presented are electric potential, $\phi$, in colors (top) and displacement, $\boldsymbol{u}$, as its magnitude (bottom) and scaled deformation (scale factor is 50000)

a moving surface wave that is visible in the scaled deformation. The displacement is localized in the IDT where the finger arrangement is placed, yet it gets "wider" showing an undesired spreading away from the IDT leading to an attenuation that is discussed further below.

Transient solution of a large model necessitate a parallel solution. The implementation is used with mpirun [60] and a preliminary analysis is conducted in order to determine the fastest solver configuration. For one time step, we measure the computation time after assembly by varying two parameters:

- The number of processors are increased varied in an increased manner for generalized minimal residual (gmres) [61] solver combined with hypre-euclid [62] preconditioner.
- The preconditioner selection is varied for gmres solver.

These variations are demonstrated in Fig. 10.

For this simulation, six processors lead to the fastest solution. A so-called overparallelization occurs such that the communication time between processors starts dominating. After setting up the number of processors, we detect that successive over-relaxation (sor) preconditioner performs the best. Therefore, the solver configuration is gmres-sor with six processors. The partitioned displacement solution at 0.466 μs is illustrated with six partitions in Fig. 11.

At different locations along the propagation direction, we monitor displacements in Fig. 12 for visualizing the behavior of traveling anharmonic overtones caused by shear and twist modes. Finger type arrangement is understood as an acoustic cavity such that the undesired modes propagate other than in $x_1$ direction and lead to their dissipation at the boundaries of the domain—for such a "leaky" wave [63], this design is described "energy trapped" [64]. Therefore, the wave demonstrates an attenuation such that the amplitude in $u_1$ decreases. Despite this attenuation caused amplitude decay is also called "propagation loss," we emphasize that the amplitude decrease is not related to a viscous dissipation. This result is supported by observing no phase change in different directions. The amplitude decay for a propagation along one direction is spread to different directions away from the IDT. All amplitudes and characteristics of $u_1$, $u_2$, and $u_3$ are analogous to the ones in Fig. 7. Overall displace-

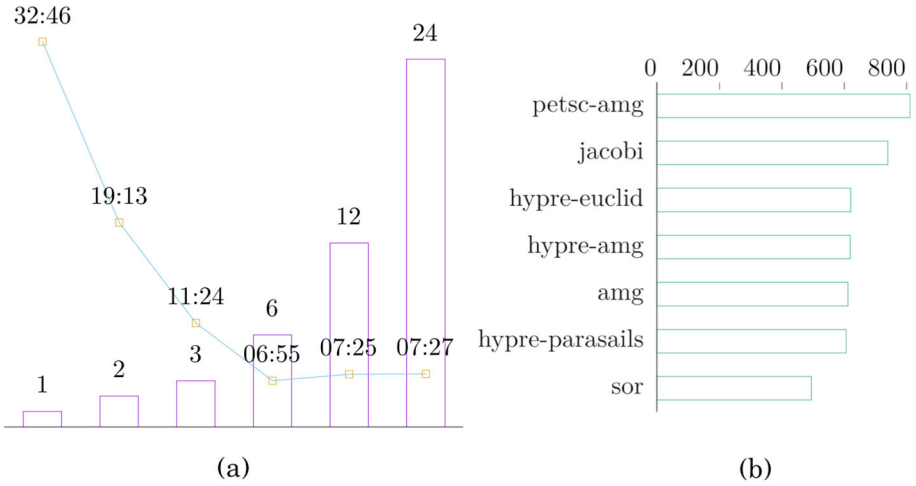


**Fig. 10** For the full scale model in one time step: **a** solution time in minute of gmres and hypre-euclid combination with 1, 2, 3, 6, 12, 24 threads (every thread runs on one Intel Xeon E7-4850 with 40 MB cache) **b** in case of six processors, the solution time variation for different preconditioners all with gmres solver

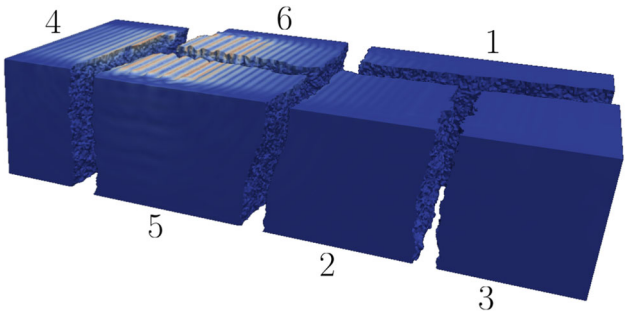


**Fig. 11** Parallelized partitions in the transient solution of the full sensor, for the sake of visualization, solutions at different threads are separated in space, the image is created by Paraview and Gimp

ment pattern indicates dominance of the Love wave mode but we stress that other undesired modes exist as well. Hence, a direct numerical simulation is of importance to verify the obtained optimal values.

## 4 Discussion

Results prove that the suggested methodology is working adequately for performing computations with varying geometries and thus properties. Computational optimization is often not feasible since numerical simulation may fail with instabilities due to varying parameters. A robust implementation is beneficial; herein, the static condensation method is of importance to obtain a robust numerical implementation. The reason is that the eigenvalue problem is attempting to detect the frequencies where inertia becomes dominant. The mass matrix in Eq. (21) has vanishing components for electric potential. This fact is related to the gauge condition (rate of electric potential) that is not restricted in the formulation. Hence, it is possible to eliminate this line from the eigenvalue problem as in Eq. (25) increasing the robustness of the system by exploiting solvers using the sparsity of the matrices. For several frequencies, a mixed mode is visible where a shear and normal wave is propagating at the same time. As the eigenvalue problem captures the deformation vector direction correctly but not the amplitude, a mixed mode is difficult to separate into Rayleigh and Love type waves. Therefore, we have performed a transient simulation in the RVE for comprehending the true nature of the surface acoustic wave.

The application herein is performing an optimization by changing the thickness parameter. This parameter is an important design variable that is usually determined by experimental trials. Not only such an optimization procedure is costly—prototype manufacturing and experimental characterization are the largest sums in product development—but a trial-and-error based approach has no guarantee that the determined value is the "best" value at all. The proposed method uses a simplification for mass sensitivity. In general, the sensor is detecting a frequency shift, which is related to the added mass on the functionalized surface. This addition of mass is due to the agents collocating on the surface such that they form a layer by adding a mass to the system and altering its inertia. Here we use a direct analogy and vary the thickness that is indeed adding a mass because of its own weight. The effect is the same that the mass sensitivity, in the case of an increased thickness, mimics the surface load caused by a layer of agents on the surface. Obviously, the mass density of to-be-detected agents are different (usually less) than the wave guiding layer's mass density. However, within the numerical computation's error such a distinction has been circumvented for the sake of simplification.

The difference between the supplied initial values and the converged values of the fitted parameters are in an adequate agreement in Table 3. This observation indicates the consistency between the dispersion relation provided in Eq. (40) and the FEM eigenvalues of the meshes. A transient analy-

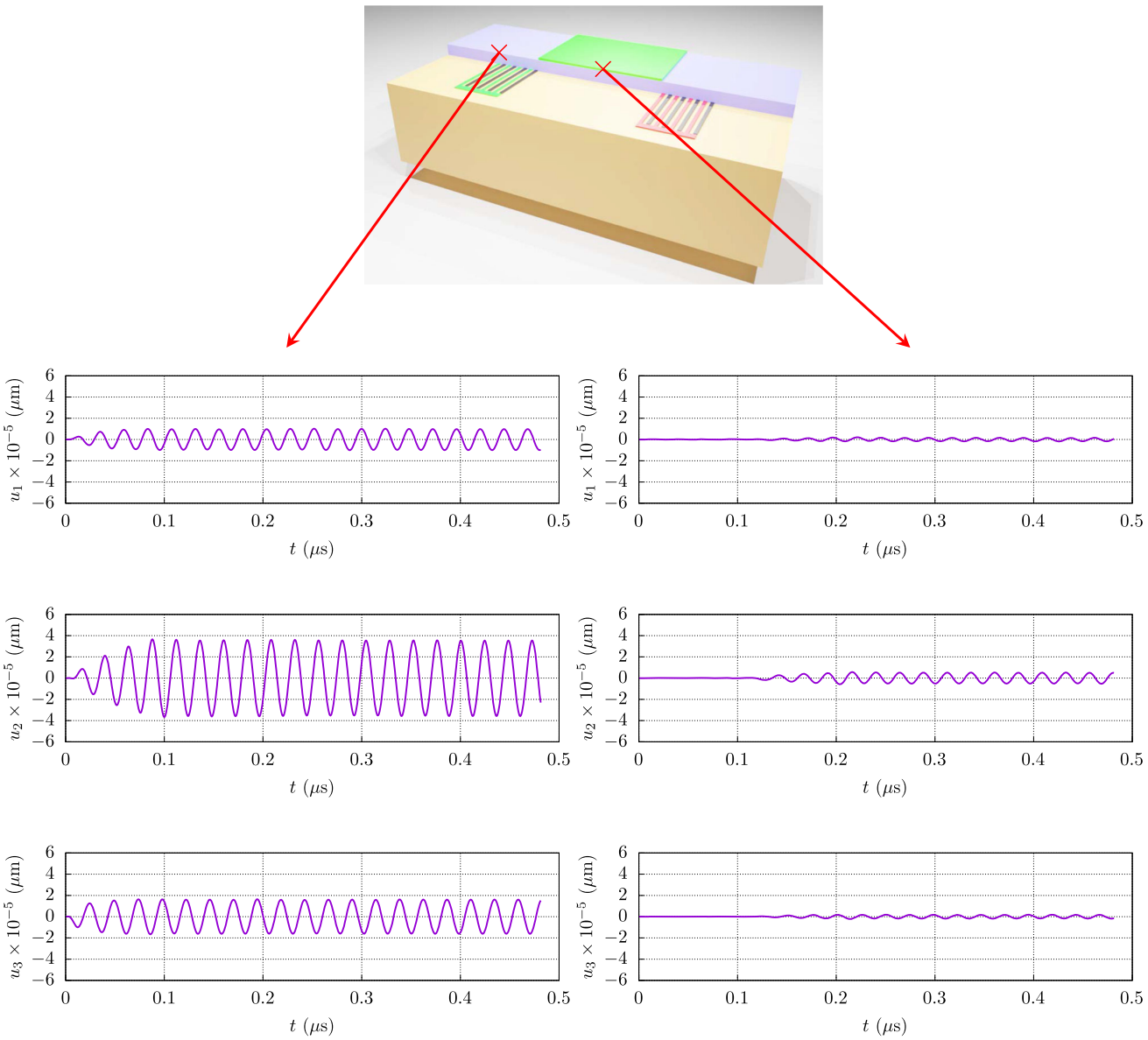


**Fig. 12** Displacement-time history monitored at locations at a distance of about 5λ on the full sensor model with the optimized values (thickness and frequency)

sis is in general necessary to verify the interpretation of the eigenvalue problem results. The transient solution, with the optimal value of thickness and frequency, revealed that the targeted Love wave has been obtained. However, undesired modes exist as well such that the maximum efficiency has not been achieved. We fail to claim that there is no possibility of creating a pure Love wave resonator in general. In general, the efficiency of such devices are measured by a quality (Q) factor that is indeed related to the attenuation effected by these mixed modes.

For this application, we refer to Fig. 1 once more, the device is sensing agents in a fluid flowing in $x_2$ direction. We emphasize the importance that there is a negligible $x_3$ displacement in order to minimize the perturbation of the fluid flow. Therefore, the design aims for a shear dominated wave, practically a Love type wave performing well in an application as demonstrated herein. The ratio of shear and thickness amplitudes varies with the thickness. Vertical motion increases for larger layer thicknesses that may cause eddy currents in the fluid leading to a performance loss by altering the mass flow of the mixture.

Cyclic deformation has been excited by the given harmonic voltage difference creating an electric field. The piezoelectric material has an instantaneous response to the electric field by deforming as we have modeled accurately. In reality, there is a viscoelastic response as well that we have

neglected for the sake of simplicity. This viscous response, the case of a rheologically simple and linear material, causes a shift in the response and for the same frequency this shift fails to alter the mass sensitivity. However, there is a dissipation in the system reducing the deformation in different directions as well as the overall performance such that the aforementioned Q-factor measures this dissipation as well. Only a computational study allows to isolate such effects in this complex system. Owing to the cyclic nature of the deformation, this dissipation is expected to cause a fatigue and a crack initiation in the design. Such computations are possible and left to future studies.

## 5 Conclusion

Product development in transceivers is possible to optimize by computational design guidelines. Especially in Surface Acoustic Waves (SAW) based systems, the tailored choice of design parameters become of utmost importance such as layer thicknesses of multi-layered designs or orientation of anisotropic materials. For an increased efficiency, or even for drafting a new design for replacing materials, we necessitate computational design guidelines.

We have discussed the eigenvalue problem of an electromechanical problem with a piezoelectric component creating a fully coupled system. For an efficient yet robust solution of this system, we have utilized a so-called static condensation and transformed the system of equations. The new solution is more stable, we have experienced no numerical convergence problems in the optimization procedure. The nature of the proposed methodology sweeps a given interval instead of an automatized algorithm such as steepest gradient, hence, an unrealistic thickness has been circumvented in this methodology.

The optimized value is a suggestion without knowing the dynamic solution and accurately estimating the displacement amplitude. Therefore, we have solved a transient full scale problem and demonstrated the displacement amplitudes in shear, along $x_2$, and normal, along $x_3$, waves in time. Even if the thickness is fine-tuned, a purely Love wave generation is not possible by using the selected substrate orientation and other design parameters. We emphasize that the methodology herein may be extended to compute the whole design space and achieve a better design as well, certainly beneficial for the industry but of little interest in basic research.

**Acknowledgements** We would like to acknowledge the Scientific and Technological Research Council of Turkey (TUBITAK) for providing financial support to Mr. Ufuk Tan Baler as a graduate student working under the project entitled "Integrated, Scalable, Functional Nanostructures and Systems" Nr. 20AG021 www.nanosisplatform.net.

**Funding** Open access funding provided by Uppsala University.



## References

1. Tamarin O, Rube M, Lachaud JL, Raimbault V, Rebière D, Dejous C (2019) Mobile acoustic wave platform deployment in the Amazon river: Impact of the water sample on the love wave sensor response. Sensors 20(1):72
2. Liu B, Chen X, Cai H, Mohammad Ali M, Tian X, Tao L, Yang Y, Ren T (2016) Surface acoustic wave devices for sensor applications. J Semicond 37(2):021001
3. Wang X, Ji J, Yang P, Li X, Pang Y, Lu P (2022) A love-mode surface acoustic wave aptasensor with dummy fingers based on monolayer MoS2/Au NPs nanocomposites for alpha-fetoprotein detection. Talanta 243:123328
4. Gulyaev Y (1998) Review of shear surface acoustic waves in solids. IEEE Trans Ultrasonics, Ferroelectr Freq Control 45(4):935–938
5. Caliendo C, Hamidullah M (2019) Guided acoustic wave sensors for liquid environments. J Phys D Appl Phys 52(15):153001
6. Gizelli E, Stevenson AC, Goddard NJ, Lowe CR (1991) Surface skimming bulk waves: a novel approach to acoustic biosensors. In: TRANSDUCERS'91: 1991 International conference on solid-state sensors and actuators. Digest of Technical Papers. IEEE. pp. 690–692
7. Länge K (2019) Bulk and surface acoustic wave sensor arrays for multi-analyte detection: a review. Sensors 19(24):5382
8. Go DB, Atashbar MZ, Ramshani Z, Chang H-C (2017) Surface acoustic wave devices for chemical sensing and microfluidics: a review and perspective. Anal Methods 9(28):4112–4134
9. Mandal D, Banerjee S (2022) Surface Acoustic Wave (SAW) sensors: physics, materials, and applications. Sensors 22(3):820
10. Mujahid A, Dickert F (2017) Surface Acoustic Wave (SAW) for chemical sensing applications of recognition layers. Sensors 17(12):2716
11. Puiu M, Gurban A-M, Rotariu L, Brajnicov S, Viespe C, Bala C (2015) Enhanced sensitive love wave surface acoustic wave sensor designed for immunoassay formats. Sensors 15(5):10511–10525
12. Huang Y, Das PK, Bhethanabotla VR (2021) Surface acoustic waves in biosensing applications. Sens Actuat Reports 3:100041
13. Brugger MS, Schnitzler LG, Nieberle T, Wixforth A, Westerhausen C (2021) Shear-horizontal surface acoustic wave sensor for non-invasive monitoring of dynamic cell spreading and attachment in wound healing assays. Biosens Bioelectr 173:112807
14. Xu Z, Yuan YJ (2019) Quantification of Staphylococcus aureus using surface acoustic wave sensors. RSC Adv 9(15):8411–8414
15. Jandas P, Luo J, Quan A, Qiu C, Cao W, Fu C, Fu YQ (2020) Highly selective and label-free Love-mode surface acoustic wave biosensor for carcinoembryonic antigen detection using a self-assembled monolayer bioreceptor. Appl Surf Sci 518:146061
16. Branecka N, Yildizdag ME, Ciallella A, Giorgio I (2022) Bone remodeling process based on hydrostatic and deviatoric strain mechano-sensing. Biomimetics 7(2):59

17. Giorgio I, Galantucci L, Della Corte A, Del Vescovo D (2015) Piezo-electromechanical smart materials with distributed arrays of piezoelectric transducers: current and upcoming applications. Int J Appl Electromagn Mech 47(4):1051–1084
18. D'Annibale F, Rosi G, Luongo A (2015) Linear stability of piezoelectric-controlled discrete mechanical systems under non-conservative positional forces. Meccanica 50:825–839
19. Kwon J, Evans K, Ma L, Arnold D, Yildizdag ME, Zohdi T, Ritchie RO, Xu T (2020) Scalable electrically conductive spray coating based on block copolymer nanocomposites. ACS Appl Mater Interf 12(7):8687–8694
20. di Cosmo F, Laudato M, Spagnuolo M (2018) Acoustic metamaterials based on local resonances: homogenization, optimization and applications. General Models Non-classical Approaches Compl Mater 1:247–274
21. Casalotti A, D'Annibale F (2022) On the effectiveness of a rod-like distributed piezoelectric controller in preventing the Hopf bifurcation of the visco-elastic Beck's beam. Acta Mechanica 233(5):1819–1836
22. Barchiesi E, Wareing T, Desmond L, Phan A, Gentile P, Pontrelli G (2022) Characterization of the shells in layer-by-layer nanofunctionalized particles: a computational study. Front Bioeng Biotechnol 10:888944
23. Schaler EW, Zohdi TI, Fearing RS (2018) Thin-film repulsive-force electrostatic actuators. Sens Actuat, A 270:252–261
24. Auld BA (1973) Acoustic fields and waves in solids. Рипол Классик
25. Wang W, Yin Y, Jia Y, Liu M, Liang Y, Zhang Y, Lu M (2020) Development of a love wave based device for sensing icing process with fast response. J Electr Eng Technol 15(3):1245–1254
26. Rocha-Gaso M-I, Fernandez-Diaz R, Arnau-Vives A, March-Iborra C, (June 2010) Mass sensitivity evaluation of a Love wave sensor using the 3D Finite Element Method. In: (2010) IEEE international frequency control symposium. IEEE, Newport Beach, CA, USA, pp 228–231
27. Du J, Harding G, Ogilvy J, Dencher P, Lake M (1996) A study of Love-wave acoustic sensors. Sens Actuat A: Phys 56(3):211–219
28. McHale G, Newton MI, Martin F (2002) Theoretical mass sensitivity of Love wave and layer guided acoustic plate mode sensors. J Appl Phys 91(12):9701
29. Gaso Rocha MI, Jimenez Y, FA, Arnau A (Mar. 2013) Love Wave Biosensors: a Review. State of the Art in Biosensors - General Aspects. Ed. by T. Rinken. InTech,
30. Shiokawa S, Moriizumi T (1988) Design of SAW sensor in liquid. Japan J Appl Phys 27(S1):142
31. Liu J, He S (2010) Properties of Love waves in layered piezoelectric structures. Int J Solid Struct 47(2):169–174
32. Logg A, Mardal K-A, Wells G eds. (2012) Automated solution of differential equations by the finite element method: The FEniCS Book. en. Vol. 84. Lecture notes in computational science and engineering. Springer, Berlin and Heidelberg
33. Downs RT, Hall-Wallace M (2003) The American Mineralogist crystal structure database. Am Mineral 88(1):247–250
34. Abali BE (2017) Computational Reality. en. Vol. 55. Advanced Structured Materials. Springer, Singapore
35. Abali BE, Reich FA (2017) Thermodynamically consistent derivation and computation of electro-thermo-mechanical systems for solid bodies. Comput Methods Appl Mech Eng 319:567–595
36. Abali BE, Queiruga A (2019) Theory and computation of electromagnetic fields and thermomechanical structure interaction for systems undergoing large deformations. J Comput Phys 394:200–231
37. Rybyanets AN, Rybyanets AA (2011) Ceramic piezocomposites: modeling, technology, and characterization. IEEE Trans Ultras, Ferroelectr Freq Contr 58(9):1757–1773
38. Bavencoffe M, Tembhurnikar N, Negulescu B, Wolfman J, Feuillard G (2018) Modelling and experimental measurements of the mechanical response of piezoelectric structures from millimetre to micrometre. Adv Appl Ceram 117(5):285–290
39. Bouchy S, Zednik RJ, Bélanger P (2022) Characterization of the elastic, piezoelectric, and dielectric properties of lithium niobate from 25° C to 900° C using electrochemical impedance spectroscopy resonance method. Materials 15(13):4716
40. Nasedkin A, Nassar ME (2022) Comprehensive numerical characterization of a piezoelectric composite with hollow metallic inclusions using an adaptable random representative volume. Comput Struct 267:106799
41. Abali BE (2022) An introduction to piezoelectric and thermoelectric materials. In: Gupta R (ed) Handbook of energy materials. Springer Nature, Singapore, pp 1–18
42. Abdollahi A, Vásquez-Sancho F, Catalan G (2018) Piezoelectric mimicry of flexoelectricity. Phys Rev Lett 121(20):205502
43. Shu L, Liang R, Rao Z, Fei L, Ke S, Wang Y (2019) Flexoelectric materials and their related applications: a focused review. J Adv Ceram 8:153–173
44. Liang X, Yu Y, Liu R, Liu W, Shen S (2022) Flexoelectricity in periodically poled lithium niobate by PFM. J Phys D: Appl Phys 55(33):335303
45. Yang H, Abali BE, Müller WH, Barboura S, Li J (2022) Verification of asymptotic homogenization method developed for periodic architected materials in strain gradient continuum. Intl J Solid Struct 238:111386
46. Vazic B, Abali BE, Newell P (2023) Generalized thermomechanical framework for heterogeneous materials through asymptotic homogenization. Contin Mech Thermodyn 35(1):159–181
47. Liu Y, Müller WH, Abali BE (2023) Dissipative mechano-electromagnetism simulations in electronic components. In: Sixty shades of generalized continua: dedicated to the 60th birthday of Prof. Victor A. Eremeyev. Ed. by H. Altenbach, A. Berezovski, F. dell'Isola, and A. Porubov. Springer International Publishing, Cham pp. 463–478
48. Liu Y, Abali BE, Eremeyev V (2023) Prediction of dissipation in electronic components by computing electromagnetism. In: Altenbach H, Bruno G, Eremeyev VA, Gutkin MY, Müller WH (eds) Mechanics of heterogeneous materials. Springer International Publishing, Cham, pp 369–383
49. Allik H, Hughes TJR (1970) Finite element method for piezoelectric vibration. Int J Numer Method Eng 2(2):151–157
50. Gaudenzi P, Bathe K-J (1995) An iterative finite element procedure for the analysis of piezoelectric continua. In: Journal of intelligent material systems and structures 6.2 (1995). Publisher: TECHNOMIC PUBLISHING CO., INC. 851 New Holland Ave., Box 3535, Lancaster, PA, pp. 266–273
51. Hernandez V, Roman JE, Vidal V (2005) SLEPc: a scalable and flexible toolkit for the solution of eigenvalue problems. ACM Trans Math Softw 31(3):351–362
52. Lehoucq RB, Sorensen DC, Yang C (1998) ARPACK users' guide: solution of large-scale eigenvalue problems with implicitly restarted Arnoldi methods. SIAM
53. Hernandez V, Roman JE, Tomas A, Vidal V (2009) A survey of software for sparse eigenvalue problems. Tech. rep. STR-6. Available at https://slepc.upv.es. Universitat Politècnica de València
54. Kushibiki J, Takanaga I, Arakawa M, Sannomiya T (1999) Accurate measurements of the acoustical physical constants of LiNbO/sub 3/ and LiTaO/sub 3/ single crystals. IEEE Trans Ultrason, Ferroelectr Freq Control 46(5):1315–1323
55. Filipovic L (2012) Topography simulation of novel processing techniques. PhD thesis. Technische Universität Wien

56. Geuzaine C, Remacle J-F (2020) A three-dimensional finite element mesh generator with built-in pre-and post-processing facilities. Int J Numer Methods Eng 11:79
57. Wang Z, Cheeke JDN, Jen CK (1994) Sensitivity analysis for Love mode acoustic gravimetric sensors. Appl Phys Lett 64(22):2940–2942
58. McHale G, Newton MI, Martin F (2002) Layer guided shear horizontally polarized acoustic plate modes. J Appl Phys 91(9):5735–5744
59. Salome version 9.9.0 Release Notes. Available at http://files.salome-platform.org/Salome/Salome9.9.0/SALOME_9_9_0_Release_Notes.pdf. SALOME Platform. (June 2022)
60. Message Passing Interface Forum. MPI: a message-passing interface standard version 4.0. (June 2021)
61. Saad Y, Schultz MH (1986) GMRES: a generalized minimal residual algorithm for solving nonsymmetric linear systems. SIAM J Scient Stat Comput 7(3):856–869
62. Falgout RD, Jones JE, Yang UM (2006) The design and implementation of hypre, a library of parallel high performance preconditioners. In: Numerical solution of partial differential equations on parallel computers. Springer. pp. 267–294
63. Campbell JJ, Jones WR (1970) Propagation of Surface Waves at the Boundary Between a Piezoelectric Crystal and a Fluid Medium. In: IEEE transactions on sonics and ultrasonics SU-17, pp. 71–76
64. Ballato A, Lukaszek T (1980) Waves in piezoelectric crystals for frequency control and signal processing. Guid-Wave Opt Surf Acoust Wave Dev, Syst Appl 239:162–169